Article

Accelerated Discovery of Perovskite-Inspired Materials through Robotized Screening Including Solar Cell Characterization

Allan Starkholm, Lars Kloo, and Per H. Svensson*
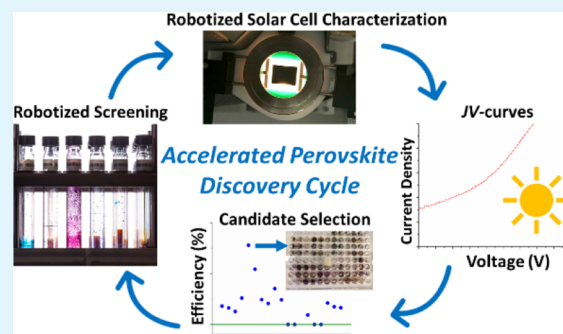
Read Online

ACCESS | 📊 Metrics & More | 📖 Article Recommendations | 🔳 Supporting Information

ABSTRACT: Currently, there is a strong need to accelerate development of systematic and robotized procedures for discovery of photovoltaic materials in order to aid the transition toward the use of clean and sustainable energy sources. Perovskite-type materials represent a broad class of compounds that have recently attracted great interest for application as photovoltaic materials. Such materials offer a vast chemical and structural space, qualifying them as an interesting starting point for further exploration using robotized screening methods. In this work, the development and application of a robotized procedure for the screening and solar cell characterization of perovskite-inspired materials is presented. Several combinations of cationic dyes and metal halides were examined by using a fully automated robotic screening cycle, including solar cell characterization based on triple mesoscopic solar cell devices. It is shown that the presented methodology is promising for the detection of new photovoltaic materials, which is demonstrated by the discovery of a selection of photovoltaic candidates. Some of the discovered candidates, for instance $[QR][PbI_3]$, were further characterized theoretically and experimentally.

KEYWORDS: robotized screening, material discovery, perovskite solar cells, automated solar cell characterization, low-dimensional perovskites
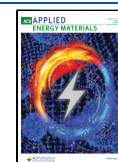
■ INTRODUCTION

Metal halide perovskites represent a class of materials that have received extensive attention the past decade owing to their impressive power conversion efficiencies (PCEs) when employed as absorber layers in solar cell devices.[1] Perovskites constitute a broad class of materials. The most commonly used ones in photovoltaics are metal halide perovskites. These have the general composition ABX_3 (A = monovalent cation, B = divalent metal cation, and X = Cl^-, Br^-, or I^-), where the A-site usually is methylammonium ($CH_3NH_3^+$) or another small organic cation, the B-site is Pb^{2+}, and the X is typically iodide (I^-).[2] The metal halide perovskites that have been applied as thin-film absorber layers in perovskite solar cells (PSCs) are materials characterized by 3D structures, where octahedral, inorganic, PbX_6 units share corners through the bridging halides.[2] The cavities formed by this connectivity are then occupied by the A-site cations.[2] Since the first report of the application of the standard 3D perovskite, $MAPbI_3$, as the absorber layer in a dye-sensitized solar cell (DSSC) in 2009, the PCEs of PSCs have dramatically increased from about 4% to well above 20% in an amazingly short time.[1,3,4] PSCs are thus one of the most rapidly growing photovoltaic technologies. Despite the impressive rise of the PSCs, there are currently two challenges impeding their large-scale commercialization. The first challenge concerns the toxicity of lead that most metal halide perovskites are based on, which

is currently extensively investigated.[5−8] This is a concern that needs to be addressed in order to show that PSCs are feasible as a future solar cell technology.[9−11] The second challenge concerns the poor stability of the standard 3D perovskite material upon exposure to air, moisture, light, and heat.[11−15] All these factors may cause rapid degradation of the perovskite material, which results in a significant and fast drop in PCE. Strategies to mitigate these issues are currently hot topics in the PSC research field.[16,17] Some of these strategies include metal substitution (Sn^{2+}, Bi^{3+}, Sb^{3+}), use of mixed composition perovskites, interface passivation, and improved encapsulation.[16−21] Efforts to improve the stability of Pb-based perovskites while also retaining high efficiencies are currently many; however, no major breakthrough in this regard has so far been demonstrated. While there are numerous novel perovskite materials reported, none of them are comparable to the standard perovskites in terms of PCEs. Another emerging research branch within the PSC field is low-dimensional perovskites.[22−24] The allowed A-site cation sizes for 3D metal

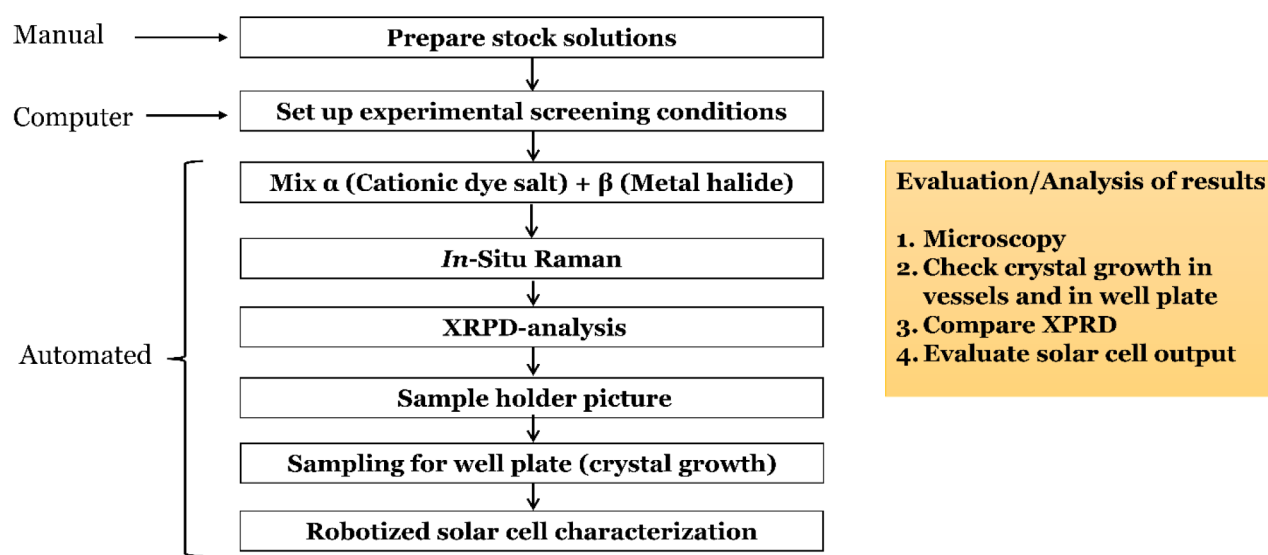## Robotized Screening and Solar Cell Characterization Workflow

Figure 1. A graphic representation of the automated robotized screening and solar cell characterization workflow used in this work. Details on the Proteus robot and the screening procedure, as well as videos demonstrating the screening operation, can be accessed in our previous report on automated robotized screening of perovskite-type materials.[37]

halide perovskites can be described using the Goldschmidt tolerance factor.[25,26] Larger cations result in a reduction of the dimensionality, leading to the formation of either 2D, 1D, or 0D perovskite-type inorganic networks.[27] The chemical and compositional space of these low-dimensional perovskites is vast and allows for incorporation of various functionalities.[22−24,27] More importantly, low-dimensional perovskite materials demonstrate significantly better stability as compared to the 3D ones.[22−24,27] Therefore, low-dimensional materials have become attractive prospects in fields such as LEDs and photovoltaics. On the other hand, the inorganic perovskite network is responsible for the semiconducting properties of the perovskites. As the perovskite dimensionality reduces, compounds with larger band gaps and inferior charge-transport properties emerge in comparison to the 3D counterparts, which is not optimal for photovoltaics.[28,29] The combination of a vast chemical space of low-dimensional perovskites and the need to accelerate the transition toward renewable energy sources makes it necessary to develop and apply search methods, which enable screening and characterization of novel energy materials in a high-throughput manner.[30,31] The timeline for the commercialization of solar cell technologies from the time of invention has proven problematically long as compared to other technologies.[32] For this purpose, automated robotized screening, synthesis, and characterization may significantly accelerate the search for new and suitable candidate materials. In the perovskite field, there have been recent attempts incorporating robotics and machine learning methods to perform synthesis more efficiently and to identify new, interesting perovskite material compositions.[33−36] While many of these efforts are promising, none of them are fully automated. Ideally, using automated robotized methods to accelerate the identification of new materials would pose positive effects on the human resources in terms of safety and the fact that more focus can be concentrated on idea generation, research design, and data analysis. Our group recently reported the use of an automated, robotized screening system to synthesize novel, low-dimensional, perovskite-type materials internally sensitized with cationic dyes.[37] In this work, we demonstrate a further significant development of the robotized screening procedure, which also includes the automated robotized solar cell characterization of new candidates. This is a very important additional step to accelerate the discovery of novel, photovoltaically active, perovskite-type compounds as well as other energy-related materials. The main aim of this study is to demonstrate the methodology and its feasibility in screening new combinations of cationic dyes and metal halides to identify novel low-dimensional, intrinsically dye-sensitized perovskite-type materials. Simultaneously, an important objective within this work is to address the poor charge-transport properties of low-dimensional perovskites by screening different cationic dyes.

■ RESULTS AND DISCUSSION

Screening Workflow. In our previous study, it was demonstrated that the identification of novel crystalline phases can be achieved by a set of specific robotized characterization tools.[37] However, it would be desirable to add additional characterization steps in the robotic screening cycle to facilitate the identification of promising candidate materials. Since the purpose in this work is to demonstrate a robotic platform for the identification of candidate materials for photovoltaics, robotized solar cell characterization represents the most strategic tool to be amended. Therefore, the robot system was developed to incorporate equipment for robotized solar cell characterization. The new screening workflow used is illustrated in Figure 1. In order to enable cheap, fast, and accurate screening and evaluation, it is necessary to use a suitable solar cell device architecture compatible with robot workflows. Furthermore, it is essential that solar cell characterization can be performed without the use of vacuum-based methods. Triple mesoscopic, carbon-based, solar cell substrates
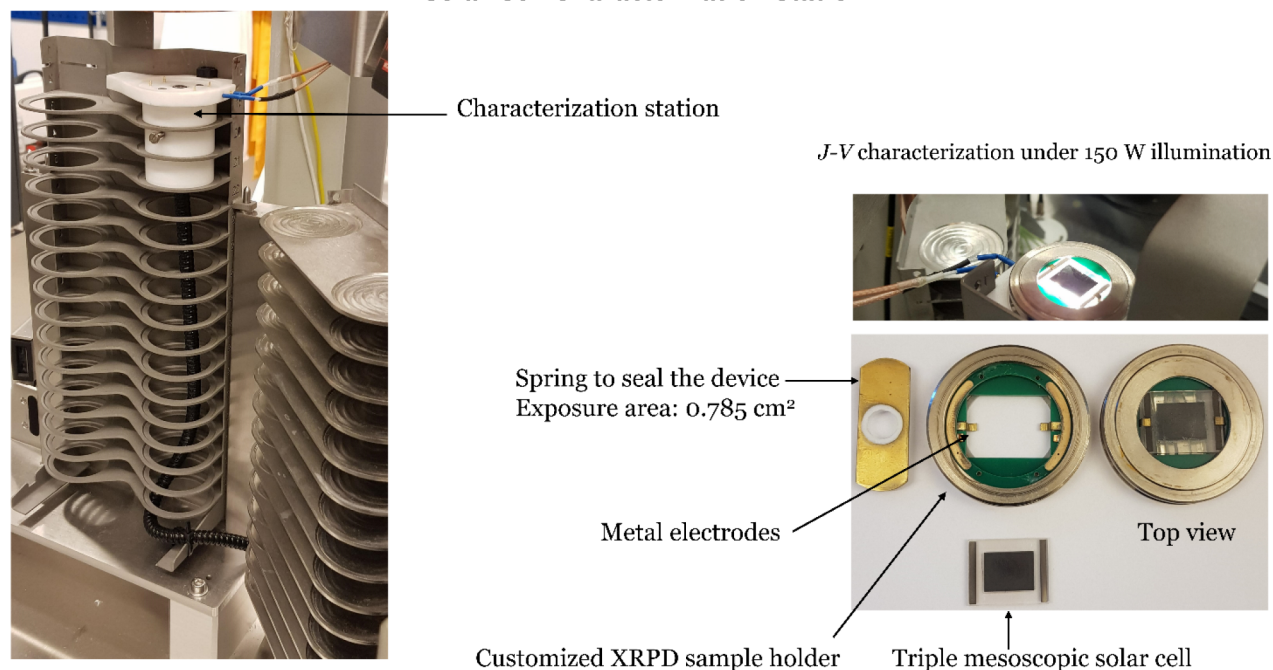
Figure 2. Illustration of the solar cell characterization station used in the robotized $J{-}V$ investigation.

fulfill these criteria.[38] The device architecture is FTO/*cp*-TiO$_2$/*mp*-TiO$_2$/*mp*-ZrO$_2$/carbon. The porous device layers allow solution deposition and subsequent crystallization as a final step prior to solar cell characterization. Triple mesoscopic perovskite devices typically offer significantly lower PCEs in comparison to PSCs based on standard architectures (e.g., FTO/*cp*-TiO$_2$/*mp*-TiO$_2$/perovskite/Spiro-OMeTAD/Au). This is generally attributed to the thick premade mesoscopic device layers (a few microns) and poor energy level matching of the substrate materials used.[38,39] Despite these limitations, the triple mesoscopic solar cell devices will constitute a good test device for screening studies since they allow efficient deployment of new materials or material precursors into a device structure highly suitable for screening and at the same time allowing the identification of materials with significant photoresponse. Triple mesoscopic electrodes with the dimensions 25 $\times$ 20 mm^2 were used in the screening investigations. These electrodes fit into standard X-ray powder diffraction (XRPD) sample holders incorporated in the robot system, and these were modified to accommodate both metal electrodes and the triple mesoscopic substrates in such a way that these can be placed onto the metal electrodes of the customized sample holder (Figure 2). An external trigger was designed for recording $J{-}V$ curves of triple mesoscopic solar cell devices. The solar cell characterization is automatically triggered when the robot places the customized XRPD sample holder containing the solar cell device on the characterization station, whereby $J{-}V$ curves are recorded and stored. The characterization station is designed with a fiber-optic cable linked to a 150 W halogen lamp through a predrilled hole. The solar cell device is placed such that the glass side coated with the device layers is positioned upward. In this way, the devices can be illuminated from underneath.[40] The halogen lamp used has a different spectral output as compared to the solar irradiation, with a particularly and nonideal large output at longer wavelengths (>600 nm). However, it is deemed to be

sufficiently good for a swift initial identification of candidate materials. Further developments with regard to the light source will become a future direction to pursue in order to better match the solar spectrum. In the screening cycle, the workflow was designed to initially mix solutions from a library containing different cationic dyes and metal halides in the stoichiometric ratios of 1:1, 1:2, and 2:1, respectively. The library of organic cations used in this study involves structurally different cationic dye halide salts, with light absorption approximately between 500 and 700 nm. These were selected to complement the light absorption of the expected anionic metal halide networks in the low-dimensional perovskite components. In our previously reported work employing robotized screening, an interesting low-dimensional, perovskite-type material based on a cationic dye was discovered.[37] This material showed a unique electronic structure, which stimulates the further exploration of such cations. In this study, the screening library is therefore expanded to accommodate cationic dyes previously unexplored for perovskites, i.e., not reported in the crystal structure database. Another important factor in cation selection is that they should be commercially readily available. There are two main ideas behind the new robotic screening.

The first is to demonstrate the newly developed solar cell characterization feature and its feasibility for future and extended use. The second is to, in the process, also discover new potentially interesting candidates based on their photovoltaic performance. Figure S2 illustrates the organic cations that were selected for the screening investigations. The stock solutions were prepared at concentrations 0.1−0.3 M in DMF/DMSO (90:10) unless otherwise stated. After the solutions of the cationic dyes are mixed with those of the metal halides, the workflow proceeds to the characterization steps within the analytical chain, which are designed to initially determine whether a new crystalline phase has formed or not. These steps include the use of *in situ* Raman spectroscopy, XRPD, and solution sampling in well plates for crystal growth. The
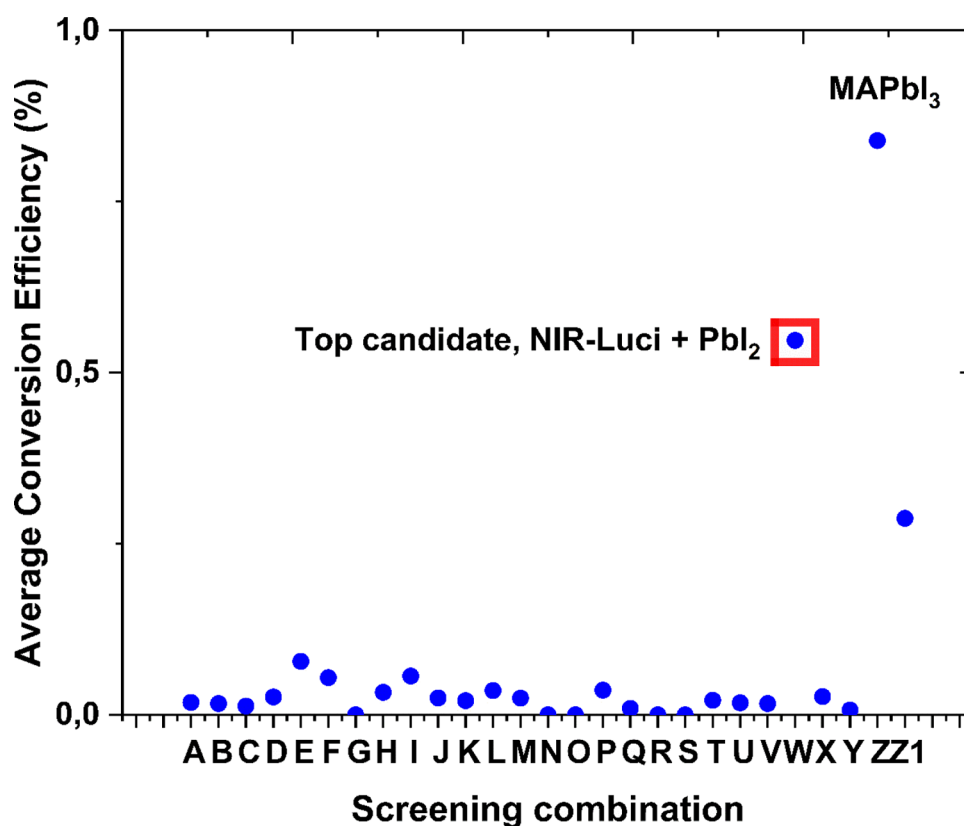
Figure 3. Example of photovoltaic output from robotized J−V characterization. Information regarding the screening combinations evaluated (A−Z) and the photovoltaic performance can be accessed in Table S2 in the Supporting Information.

Table 1. Summary of the Photovoltaic Data Obtained from a Selection of the Materials and Material Combinations Investigated in This Work[a]

system	device architecture	J_{SC} (mA/cm^2)	V_{OC} (V)	FF	PCE (%)
1: MAPbI$_3$ (average, robotized dispension)	triple mesoscopic	2.18 ± 0.442	0.577 ± 0.234	0.409 ± 0.224	0.839 ± 0.423
2: MAPbI$_3$ (champion, robotized dispension)	triple mesoscopic	3.13	0.617	0.415	1.61
3: MAPbI$_3$ (average, manual dispension)	triple mesoscopic	1.59 ± 0.2	0.7 ± 0.008	0.279 ± 0.019	0.624 ± 0.112
4: MAPbI$_3$ (champion, manual dispension)	triple mesoscopic	1.89	0.687	0.298	0.775
5: NIR-Luci+PbI$_2$ (average)	triple mesoscopic	1.24 ± 0.442	0.528 ± 0.035	0.4 ± 0.052	0.547 ± 0.252
6: NIR-Luci+PbI$_2$ (champion)	triple mesoscopic	1.87	0.575	0.486	1.04
7: [QR][PbI$_3$] (average)	standard PSC	0.654 ± 0.048	0.659 ± 0.055	0.367 ± 0.024	0.158 ± 0.016
8: [QR][PbI$_3$] (champion)	standard PSC	0.686	0.675	0.393	0.182
9: QR+SbI$_3$ (average)	standard PSC	0.935 ± 0.274	0.088 ± 0.08	0.230 ± 0.133	0.0321 ± 0.031
10: QR+SbI$_3$ (champion)	standard PSC	1.18	0.170	0.321	0.0645

[a]The average values and standard deviations for systems **1**, **3**, **5**, **7**, and **9** are based on 6, 5, 13, 6, and 4 cells, respectively.

screening cycle and its decision-making chain has previously been covered in more detail.[37] The newly added feature in this work is the robotized solar cell characterization, with the purpose of identifying photovoltaically promising candidates. Furthermore, the new robot component is modular and could be used separately for a high-throughput type of photovoltaic screening. This novel screening workflow was designed to identify new crystalline materials in a relatively swift manner and facilitate the selection of material candidates for solar cell application. Once a screening cycle is finished, the output data are analyzed and some materials are further characterized manually.

Robotized Solar Cell Evaluation. An example output of the robotized solar cell characterization based on triple mesoscopic devices is visualized in Figure 3. From here, one screening combination emerged as the top candidate (W),

displaying a promising photovoltaic output. The top candidate is based on the combination 2-[(1E,3E)-4-[4-(dimethylamino)phenyl]-1,3-butadien-1-yl]-4,5-dihydro-(4S)-4-thiazolecarboxylic acid hydrochloride salt (hereafter abbreviated NIR-Luci) + PbI$_2$, displaying an average PCE of around 0.5% (Table 1). In order to evaluate the feasibility of the robotized solar cell characterization methodology, the standard MAPbI$_3$ perovskite was also included in the screening study for comparison: A series of robotized J−V measurements on samples precipitated from a 0.5 M DMF solution of MAPbI$_3$, using the robot system, was performed and subsequently analyzed. These experiments based on the MAPbI$_3$ perovskite yielded an average PCE of about 0.8% (Table 1), which indeed indicates that the method can identify a photovoltaic materials candidate. The PCEs recorded are clearly far away from the top ones recorded for MAPbI$_3$, but any new candidate material

is likely to produce a signal well above the noise level. In addition, the champion MAPbI$_3$-based device displayed a PCE of approximately 1.61% (Table 1 and Figure S3). It should be noted that the robotized solar cell characterization is performed at ambient conditions, which is not ideal for the MAPbI$_3$ perovskite material, considering its sensitivity to moisture and oxygen. However, the obtained results highlight the feasibility of the robotized screening workflow also for materials that are usually considered sensitive under ambient conditions. In order to shed some further light on the reliability of the robotic workflow, additional $J{-}V$ comparisons on the MAPbI$_3$-based cells were made through manual cell manufacturing. After an annealing step, the devices were subjected to solar cell characterization by using the equipment within the robotic platform. The results acquired from those experiments are relatively similar to the ones based on the robotized perovskite solution dispensing, displaying an average PCE of approximately 0.62% (Table 1). This is slightly lower than the average of the ones produced by the robotic workflow, a result that may indicate a performance advantage by automated device manufacturing. The standard deviation of the PCEs from devices based on the robotic workflow is slightly higher than those based on manual dispensing (Table 1), which may result from somewhat longer times between solution deposition and solar cell characterization during the robotic screening.

In this context, we should not forget that the low PCEs recorded in these experiments can be attributed to the primitive light source regarding both light intensity and spectral distribution. For instance, a significantly better photovoltaic performance of the MAPbI$_3$-based cells under 1 sun illumination has previously been demonstrated.[41] As mentioned above, the top candidate from the screening of cationic dyes with metal halides is the combination of NIR-Luci + PbI$_2$ (Figure 3). The champion device displayed an encouraging PCE of 1.04% (Figure S3), which is on par with the MAPbI$_3$ perovskite (Table 1). NIR-Luci is a luciferin-type cationic dye with a near-infrared emission around 700 nm, making it complementary to the absorption range of the low-dimensional perovskite-type framework. The fact that such a significant photovoltaic output could be detected for this type of material combination with the current robotized approach is strongly indicative of its potential for future application. This material candidate is consequently of great interest for further investigation. In addition, the same cation mixed with bismuth iodide (screening combination Z-1) yielded the second highest photovoltaic performance (0.287%, Figure 3) among the investigated screening combinations, which further indicates that mixtures of this cationic dye and different metal halides may be of great interest for further analysis. Moreover, it is evident from Figure 3 that most screening combinations produced an intermediate PCE. A few screening combinations produced a higher photovoltaic output, thereby calling for a deeper analysis. One is the screening combination E (Figure 3), quinaldine red (QR) + SbI$_3$ (1:1), which yielded an average PCE of 0.078% (Table 1). Considering the limited spectral output of the illumination source used in combination with the absorption range of the dye (absorption maximum around 530 nm) and the thick device layers, this result is strongly encouraging. Furthermore, the two other screening combinations, F (2:1) and I (1:2), of the same components, QR and SbI$_3$, yielded slightly lower but still significant PCEs, 0.054 and 0.057%, respectively (Table 1). The observation that the 1:1

screening combination produced a higher photovoltaic performance may indicate a better synergy or interaction between the cationic dye and the iodoantimonate backbone. Another screening combination demonstrating an intermediate PCE was A, QR + PbI$_2$. The resulting PCE was 0.018% (Table 1), and in addition, this screening combination resulted in the growth of crystals suitable for single-crystal X-ray diffraction (SXRD) studies, which enabled the crystal structure determination. Thus, far, this is the only screening combination where the crystal structure could be fully elucidated. The crystal structure of this material will be discussed further in the following section. As previously outlined, the light source used within the current robotized solar cell characterization setup significantly deviates from the solar spectrum and will therefore likely result in a slightly underestimated photovoltaic performance. Therefore, we investigated some of the intermediately performing screening combinations using a conventional (noninverse) PSC device architecture for solar cell characterization under AM1.5 solar simulator illumination (intensity 100 mW/cm^2) to shed some light on the photovoltaic potential of these candidates, as well as to get insights into potential improvements of the robotic setup. The lead-free alternative, screening combination E, and the screening combination A, for which the crystal structure could be determined, were selected for this purpose. The latter combination constitutes a valuable example for comparison, since it allows a discussion of the relation between the photovoltaic performance and structure. Furthermore, this material was characterized by means of quantum chemical calculations in order to elucidate its electronic structure. The crystal and electronic structure of the screening combination A, as well as the solar cell characterization based on the standard PSC architecture, will be discussed in the following sections.

Overall, the results of the robotized solar cell characterization experiments display variation with respect to the different material combinations (Figure 3 and Table S2). Some screening combinations, such as G, N, O, R, and S did not yield any significant photovoltaic response (Table S2). A few other screening combinations based on cationic dyes with absorption ranges of 600−700 nm yielded either low or intermediate PCEs (J, K, L, M, X, and Y, respectively; Table S2). The fact that there is a considerable variation in the results provides strong support for the robotized screening approach, since promising combinations quite clearly can be identified for deeper analysis. In summary, the robotic screening cycle is demonstrated to be an excellent tool for the screening of new, perovskite-type, photovoltaic materials. After initial preparation work (making stock solutions, experimental design, etc.), the robot can perform a fully unsupervised screening. From the point of experimental submission and initiation of the screening process, it takes about 35 min per sample to undergo a full screening and characterization cycle. Assuming that one performs a screening of 10 cationic dyes and five metal halides (which approximately represents one screening run in this work) for one stoichiometric ratio, this would amount to 50 reactions (mixing, crystallization, and subsequent material and ultimate device characterization). Such a screening would be completed within a day with the robot, a nonrealistic task for a single human being. Expanding this to two additional stoichiometric ratios would as a consequence require about 3 days of robotized work. The total time could in principle differ depending on the purpose of the screening. From a time perspective, one limitation of the robotic system is
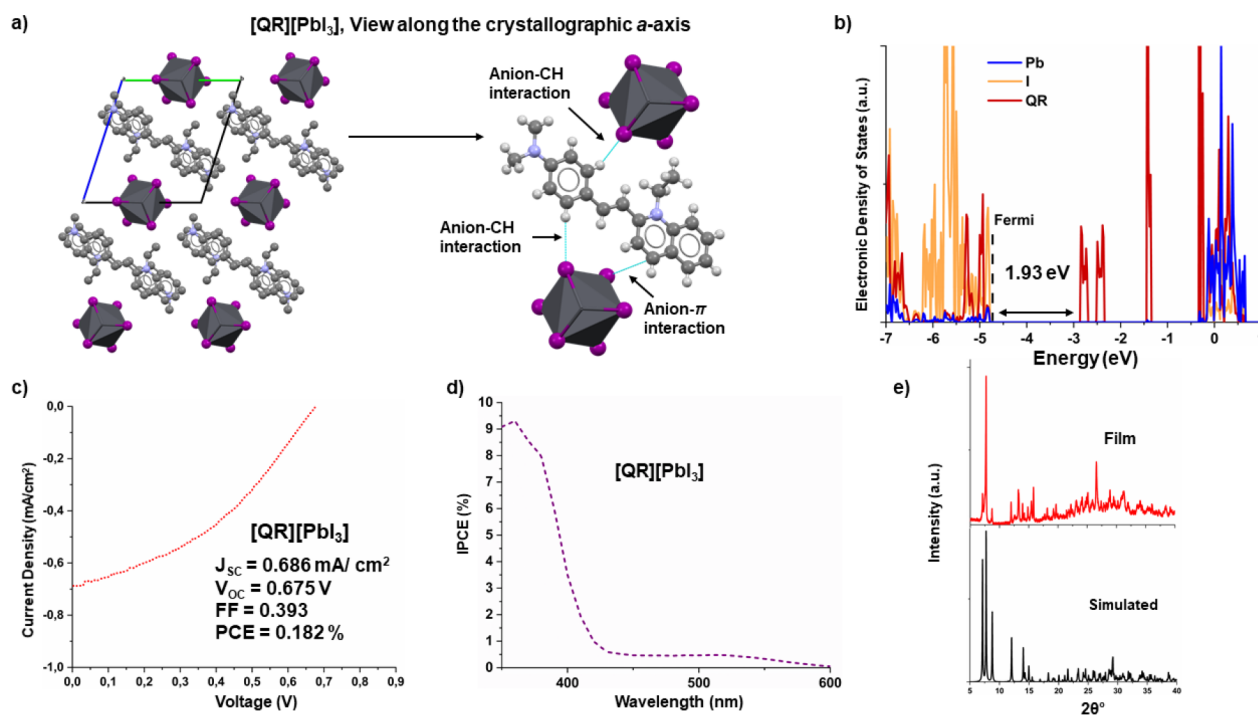
Figure 4. (a) $2 \times 2 \times 2$ super cell of $[\text{QR}][\text{PbI}_3]$ along the crystallographic a-axis and illustration of the intermolecular interactions. (b) The DoS of $[\text{QR}][\text{PbI}_3]$. (c) J–V curve of the champion device based on $[\text{QR}][\text{PbI}_3]$. (d) IPCE spectrum of a device of $[\text{QR}][\text{PbI}_3]$. (e) XRPD patterns of a film of $[\text{QR}][\text{PbI}_3]$ compared to a simulated XRPD pattern based on the crystal structure.

the solution mixing step, which currently can handle one sample at a time. For future developments, it would be desirable to extend to multichannel dispensers and modular parts that could be programmed to allow higher flexibility. The robotic system is enclosed, and a variety of solvents could be employed. Furthermore, the solution deposition onto the solar cell devices is performed by drop-casting from a needle, whereafter the substrates are allowed time to get infiltrated and thereafter characterized. A potential development could involve spin-coating and/or hot plates for controlled annealing schemes. Overall, the robotic system is versatile with the possibility to screen various materials combinations, either solely for photovoltaic characterization or by performing a full screening cycle. In summary, it has been demonstrated that the newly developed robotized screening workflow is viable for the detection of new promising photovoltaic candidate materials.

Crystal Structure of $[\text{QR}][\text{PbI}_3]$. Dark-red, needlelike crystals emerged in the well plate position from the screening combinations of QR and PbI$_2$ (both from the 2:1 and 1:1 reaction mixtures). The compound, which was found to be $[\text{QR}][\text{PbI}_3]$, crystallizes in the triclinic space group P$\bar{1}$ and consists of QR cations and 1D, infinite, anionic chains with the repeating unit $[\text{PbI}_3]^-_n$. Table S1 provides a summary of the crystal structure data. The anionic chains display face-sharing connectivity and run along the crystallographic a-axis (Figure 4a). The QR cations exhibit extensive π–π stacking running parallel to the inorganic chains. Furthermore, the cations interact with the $[\text{PbI}_3]^-_n$ framework along the stacking direction by means of anion–π, as well as anion–CH$_{\text{Arom}}$ interactions (Figure 4a).

Each cation interacts with two adjacent $[\text{PbI}_3]^-_n$ chains through such interactions, thus acting as linking units between the inorganic layers. Therefore, when accounting for the intermolecular interaction between the organic cations and the inorganic framework, the structural motif could be considered as a pseudo-2D network of alternating 1D $[\text{PbI}_3]^-_n$ chains and 1D QR stacks. The solvate-free nature of $[\text{QR}][\text{PbI}_3]$ is noteworthy, which is in contrast to our as well as other previously reported perovskite-type compounds incorporating chromophores as cations.[37] This could render better stability of the deposited thin films as compared to solvated perovskite-type materials, which show a tendency to decompose as a result of evaporation of the structurally incorporated solvent molecules. Different types of crystals from the screening combinations of QR and SbI$_3$ emerged but were too small for SXRD analysis. Work is in progress aiming to grow larger crystals of hitherto unknown phases. The crystal structure of the organic dye iodide salt, $[\text{QR}]\text{I}$, was determined as a reference for XRPD and band structure comparisons.

Electronic Structure. Band structure (Figure S4) and density of states (DoS) computations (Figure 4b) using the B3LYP hybrid functional was determined to investigate the electronic structure of $[\text{QR}][\text{PbI}_3]$. The computed band gap is 1.93 eV, which is in good agreement with the color of the compound. From the DoS of $[\text{QR}][\text{PbI}_3]$, information regarding potential electronic transitions can be extracted (Figure 4b). The top of the valence band (VB) is dominated by contributions from the iodide (I$^-$) ions of the $[\text{PbI}_3]^-_n$ chains. Moreover, there is an approximately equal contribution of energy states from the cation (QR) and iodide (I$^-$) atoms in the $[\text{PbI}_3]^-_n$ anions. The lowest unoccupied band (formally, the conduction band, CB) is located at around −2.8 eV, and it can predominantly be ascribed to the dye cation (QR). The band gap of 1.93 eV corresponds to an electronic transition from the top of the VB to the bottom of lowest unoccupied band. Overall, the electronic structure indicates a possibility for a charge transfer between the inorganic and organic entities. More in-depth studies are necessary to elucidate the

mechanisms of electron transfer and whether direct electron regeneration of the organic dye from the inorganic component is possible.[42] This will depend on the type and degree of interaction between the moieties. For reference, the computed molecular bandwidth of the organic iodide salt, [QR]I, is 1.91 eV.

Solar Cell Characterization-Standard PSC Architecture. Solar cells based on [QR][PbI$_3$] and the screening combination QR+ SbI$_3$ (in spite of its exact structure remaining unknown) were investigated by using the standard PSC device architecture of FTO/cp-TiO$_2$/mp-TiO$_2$/dye-sensitized perovskite/Spiro-OMeTAD/Au. Thin films of [QR][PbI$_3$] were deposited by spin-coating a precursor solution of the iodide salt of QR and PbI$_2$ (2:1) in DMSO at 4000 rpm. The substrates were then annealed for approximately 30 min before the final device layers were added. XRPD analysis of the annealed thin films of the precursor solution confirmed that these predominantly consist of [QR][PbI$_3$], with only minor crystalline impurities (Figure 4e). Thin films of the screening combination QR + SbI$_3$ were prepared in analogy to [QR][PbI$_3$]. Illumination of solar cell devices based on the two materials was performed by using an AMG1.5 solar simulator lamp corresponding to an intensity of 100 mW/cm^2. $J-V$ curves were subsequently recorded from the solar cell devices. Table 1 summarizes the photovoltaic results. The considerably better PCEs of the standard devices based on the compound [QR][PbI$_3$], compared to the triple mesoscopic devices, are noteworthy. The champion device displayed a PCE of 0.18%, a J_{SC} of 0.686 mA/cm^2, a V_{OC} of 0.675 V, and an FF of 0.393 (Figure 4c), which clearly shows that this material may indeed be an interesting prospect for future studies after further optimization. Equivalent measurements using the screening combination QR + SbI$_3$ employing Spiro-OMeTAD as the hole transport material (HTM) were, however, unsuccessful.

Therefore, P3HT was used as an HTM instead. At this stage, it is unknown why the combination of the Sb-containing screening product and Spiro-OMeTAD did not produce sensible results. The results when employing P3HT show a champion device PCE of 0.064%, a J_{SC} of 1.18 mA/cm^2, a V_{OC} of 0.165 V, and an FF of 0.321, which are in good agreement with the robotized solar cell characterization attempts. The photovoltaic characterization of QR + SbI$_3$ employing the standard PSC structure displayed highly differing results, and it should be emphasized that the characterization of this combination is at an early stage, and further investigations will be necessary, particularly when considering the likely existence of multiple phases. Another important factor to consider is the additional annealing step during the fabrication of the standard PSC devices, in contrast to the triple mesoscopic ones within the robotic setup. This may be of importance considering the expected temperature sensitivity of the organic cationic dyes. In the preparation of DSSCs, temperatures above 100 °C for more than a few minutes are typically avoided to prevent significant decomposition of the dye molecules.

The incident photon-to-current efficiency (IPCE) studies were performed to obtain insights into the device performance of solar cells based on [QR][PbI$_3$]. An IPCE spectrum is illustrated in Figure 4d. The IPCE spectrum depicts a photocurrent contribution up to 600 nm, where the highest IPCE is shown at wavelengths <420 nm. A small contribution can be noted between 500 and 600 nm, which indicates

electronic transitions corresponding the smallest band gap involving the dye cation (QR). This suggests involvement of unoccupied states ascribed to the dye (QR) in the photoexcitation process, either through direct HOMO−LUMO excitation of the dye or through charge transfer from the CB of the inorganic [PbI$_3$]^-_n chain to the dye LUMO (HOMO corresponds to the highest occupied molecular orbital and LUMO to the lowest unoccupied molecular orbital). The strong contribution at <420 nm may indicate the latter scenario, considering the unoccupied QR energy levels at around −2.5 and −2.9 eV, respectively. Further studies following the results in this work are therefore encouraged. The results based on [QR][PbI$_3$] indicate that, as discussed in the robotized solar cell characterization section, the photovoltaic performance based on the triple mesoscopic devices may indeed be underestimated considering the primitive illumination source. For the screening combination QR + SbI$_3$, the solar cell performance based on both the standard PSC architecture and the robotized triple mesoscopic devices are comparable, in turn highlighting the ability of the presented robotized screening and solar cell characterization procedure to identify photovoltaic candidate materials. However, it is of paramount importance to further investigate and optimize the solar cell characterization of this particular materials combination based on the standard device structure to improve its potential for photovoltaic application. As mentioned, the photovoltaic data of [QR][PbI$_3$] employing the standard architecture show significantly better performance than the robotized solar cells based on the triple mesoscopic device structure, indicating that also intermediately performing candidates may represent interesting prospects for photovoltaics. This, in turn, suggests a potential for improvement of the robotized screening and characterization workflow, possibly by incorporating other characterization methods or improving deposition methods to allow the identification of other promising candidate combinations that may otherwise be overlooked.

■ CONCLUSIONS

This work has demonstrated a proof of concept regarding a screening approach for novel materials discovery based on an automated, combined, robotized screening and solar cell characterization of perovskite-type materials with the aim of identifying promising candidate materials for photovoltaic applications. Based on the evaluation of the automated robotic workflow, which included experiments employing the standard MAPbI$_3$ perovskite, it can be concluded that the current setup and workflow represent a viable approach for this purpose. While there remain improvements to consider, the overall method applied highlights the successful identification of interesting photovoltaic candidate materials based on a triple mesoscopic solar cell architecture. This is demonstrated with the discovery of the combination of NIR-Luci and PbI$_2$, which yielded a promising PCE. Further studies and subsequent optimization will be necessary to fully realize its potential. Moreover, through automated robotized screening, a novel, low-dimensional, perovskite-type material ([QR][PbI$_3$]) was identified. This material displayed a promising conversion efficiency of close to 0.2% in a standard PSC device architecture, already before any optimization. This indicates that also intermediately performing screening combinations identified by the robotized solar cell characterization attempts may be of interest for photovoltaics. The robotized screening

procedure can be developed even further to optimize the screening cycle, for instance by adding AI and machine learning routines. Ultimately, the automated screening method presented in this work can be expanded for solar cell screening based on different materials and material combinations, not necessarily restricted to perovskite-type materials. This highlights the potential of automation to significantly accelerate the discovery and evaluation of novel materials and solar cell concepts. Finally, this work could constitute an interesting model and inspiration for further developments and advances within robotized materials discovery, as well as research in high-throughput methods.

■ EXPERIMENTAL SECTION

Robotized Screening and Solar Cell Measurement Workflow. The screening cycle starts with experimental design (choice of cations and metal halides, stoichiometries to be investigated, crystallization methods, etc.). These parameters are then submitted through computer-controlled software. Once the experiment is submitted, the screening cycle will start upon feeding the robot with barcoded reaction vessels, corresponding to the number of reactions defined. In this work, the screening workflow was designed to mix organic cationic dye salts (denoted α) and metal halides (denoted β) in stoichiometric ratios of 1:1, 1:2, and 2:1. Stock solutions of α and β were prepared in a DMF/DMSO mixture (90:10) in the concentration range 0.1−0.3 M and fed to the robot prior to the screening. The vessels were placed in thermal blocks, whereafter the robot arms started to dispense the solutions according to the experimental definition. α and β were mixed to a total volume of 1.1 mL, and the resulting solution was stirred for a predefined time, which was set to about 1 min. After the mixture was mixed, the characterization steps followed. The analytical sequence continued with *in situ* Raman measurements, XRPD (sampling of reaction solutions onto triple mesoscopic solar cell substrates was performed in this step), sampling of 100, 50, and 20 μL, respectively, of the reaction solutions into a 96-cell well plate for crystal growth, and finally solar cell characterization. After solution sampling, the customized solar cell sample holders were placed in the solar cell characterization station with a robotic gripper. The solar cell characterization station (Figure 2) consists of a white plastic body, designed to fit into the XRPD hotels of the robot system. A hole was drilled through the whole plastic body (from the bottom to the top), as shown in Figure 2). A fiber-optics cable propagating the light from a halogen lamp (USHIO DDL 20 V, 150 W) was placed within the white plastic body, such that the light exit is at the top of the drilled central hole. Furthermore, the white plastic body has two metal pins (connected to the solar cell $J−V$ testing system) sticking out from the top (Figure 2). The customized sample holder, containing a triple mesoscopic solar cell device, is positioned directly onto the metal pins by a robotic gripper to ensure contact with the metal strips of the sample holder, which, in turn, are connected to the metal electrode fingers that the solar cell device is resting on. The sample holder is held in place by a spring (right side of Figure 2). The hole on the spring is of the same size as the fiber-optics exit head and thus helps to channel and concentrate the light onto a defined area of the solar cell device. Immediately when the sample holder has been placed on the metal pins of the plastic body, the $J−V$ characteristics are recorded. During the screening cycle, the lightning in the lab is switched off to avoid stray light. The irradiance was estimated to be about 500 W/m². A video demonstration of the robotized solar cell characterization step in the robotic screening cycle can be found in https://www.youtube.com/watch?v=N20u2dC-I-k and in the Supporting Information video.

Single-Crystal Growth. [QR][PbI$_3$]: Crystallization of [QR]-[PbI$_3$] occurred in the well-plate positions after sampling 100, 50, and 20 μL of the reaction solution from the robotized screening (ratio 1:1). Dark-red, needle-shaped crystals suitable for in-house SXRD studies emerged after 24 h.

[QR]I: Dark-red crystals of [QR]I emerged in the bottom of a 10 mL vial upon evaporation of a 0.1 M DMF solution of [QR]I.

Single-Crystal X-ray Diffraction. Crystals of [QR][PbI$_3$] and [QR]I were mounted on a cryoloop using Paratone oil and subsequently placed under a cold nitrogen stream. SXRD data were recorded at 200 K using a Bruker APEXII diffractometer (Mo Kα radiation), equipped with a CCD detector. Diffraction patterns of the crystals were collected with ω- and ϕ-scans. The collected data sets were integrated with the Bruker SAINT software[43] package, and absorption correction using the Bruker SADABS program was applied. SHELXS and SHELXL, within the Bruker program package, were then used for crystal structure solution and refinement.[44] Direct methods were used for solving the crystal structures, which resolved the positions of all atoms, except hydrogen atoms. Hydrogen atoms were placed at calculated positions. The crystallographic data can be accessed free of charge at the Cambridge Crystallographic Data Centre through CCDC numbers 2099299 ([QR]PbI$_3$]) and 2099298 (the reference organic iodide salt [QR]I), respectively.

Powder X-ray Diffraction. For XRPD data collection, a PANalytical X'Pert Pro diffractometer, equipped with a Cu, long fine focus, X-ray tube, and PIXcel detector, was used. Automatic divergence, antiscatter slits and 0.02 rad Soller slits, and an Ni filter were employed during the data accumulation. Films of [QR][PbI$_3$] were deposited directly onto zero background holders (ZBHs) using spin-coating. After annealing, the ZBH plates were mounted in stainless steel holders and subsequently placed in a powder diffractometer. Subsequent data collections were performed at room temperature while spun in order to increase the randomness of the crystal sample orientations. Data collections were recorded by using scan lengths of approximately 17 min. The samples were analyzed between 2 and 40° 2θ using 255 detector channels.

Solar Cell Fabrication for Standard PSC Architecture. Fluorine-doped tin-oxide (FTO) glass substrates were cut (25 × 15 mm²), etched using zinc powder and 2 M hydrochloric acid, and cleaned prior to deposition of the different device layers. Cleaning was performed in three steps by washing the glass substrates under sonication for about 40 min, using acetone and ethanol (99.9%), and finally deionized water. A compact TiO$_2$ blocking layer spin-coating formulation (Ti-Nanoxide BL/SC, Solaronix) was subsequently spin-coated at 5000 rpm for 30 s. Afterward, the substrates were baked at 500 °C for 60 min in an oven, resulting in a compact layer thickness of 50−70 nm. In the following step, a mesoporous TiO$_2$ layer was deposited by spin-coating a colloidal TiO$_2$ solution (TiO$_2$ paste, 30 NR-D, Dyesol diluted with absolute ethanol in a 1:5.5 weight ratio) at 4000 rpm for 30 s. The substrates were annealed by using a hot plate at 80 °C for 5 min before being baked in an oven at 475 °C for 30 min. [QR]I (iodide salt of QR) and PbI$_2$ or SbI$_3$ were dissolved in a 2:1 ratio in DMSO to a concentration of 0.1 M to form the precursor solution. The solutions were stirred for approximately 30 min before being filtered using a 0.45 μm PTFE filter. The precursor solutions were spin-coated at 4000 rpm and annealed at 150 °C for 30 min. A hole-transport layer (Spiro-OMeTAD, 20 mg/mL chlorobenzene, or P3HT, 10 mg/mL chlorobenzene) was then spin-coated on top of the absorber layer at 3000 rpm (Spiro-OMeTAD) or 4000 rpm (P3HT) for 30 s. Finally, gold metal contacts were thermally evaporated at low pressure (1×10^{-6} mbar) to generate a counter electrode layer of 80 nm thickness.

Current−Voltage ($J−V$) Characterization. Solar cell characterization employing the standard PSC architecture was performed using an A Keithley 2400 electrometer to record the photocurrent. An AM 1.5G solar simulator (Newport 91160-1000) with an applied light intensity of 100 mW/cm², which was calibrated with a certified silicon reference solar cell (Fraunhofer ISE), was used as the illumination source. During measurements under illumination, the solar cells were covered with a mask with an exposure area of 0.126 cm².

Incident-Photon-to-Current Efficiency (IPCE) Investigation. The IPCE data collection was performed using an IPCE setup equipped with an ASB-XE-175 light source, a monochromator (Spectral Products CM110), and a Keithley 2700 multimeter.

Band Structure and Electronic Density of States. The band structures and the density of states were computed using the hybrid functional B3LYP within the Crystal 17 package.[45] The basis sets of I and Pb were of small-core, effective-core potential (ECP) quality (MDF28 for I and MDF60 for Pb),[46,47] and the valence space was of double-ζ quality.[48,49] In these models employing periodic boundary conditions, dye molecule cations were explicitly included at their crystallographic positions. The basis set of S was also of Stuttgart−Dresden−Cologne ECP type (MWB10) with an associated small and contracted valence space.[50] The basis sets used for C and H were of 3-21G or 6-31G quality. Band structures were constructed from the web facility, CRYSPLOT.[51] The dye molecules were studied using both Crystal 17 and the program package Gaussian 16 (rev. B.01).[52]

■ ASSOCIATED CONTENT

Ⓢ Supporting Information

The Supporting Information is available free of charge at https://pubs.acs.org/doi/10.1021/acsaem.3c02242.

> Structural data of compounds [QR][PbI$_3$] and [QR]I; 50% probability ellipsoidal models of the asymmetric unit of [QR][PbI$_3$] and [QR]I; illustration of the molecular structures of the cationic dyes in this work; table with the names and identifiers of the cationic dyes; table with the robotic screening combinations investigated and their photovoltaic output; champion device plots of the $J-V$ curves of the best screening combinations; band structure graphs of [QR][PbI$_3$] and [QR]I (PDF)

> Robotized solar-cell characterization step in the robotic screening cycle (MP4)

> Crystallization of [QR][PbI$_3$] (CIF)

> Crystallization of [QR]I (CIF)

■ AUTHOR INFORMATION

Corresponding Author

Per H. Svensson − *Chemical and Pharmaceutical Development, RISE Research Institutes of Sweden, Södertälje SE-151 36, Sweden; Applied Physical Chemistry, Department of Chemistry, KTH Royal Institute of Technology, Stockholm SE-114 28, Sweden;* ⓞ orcid.org/0000-0003-2410-7366; Email: per.h.svensson@ri.se

Authors

Allan Starkholm − *Department Solution-Processing of Hybrid Materials and Devices, Helmholtz-Zentrum Berlin, 12489 Berlin, Germany;* ⓞ orcid.org/0000-0002-2032-1966

Lars Kloo − *Applied Physical Chemistry, Department of Chemistry, KTH Royal Institute of Technology, Stockholm SE-114 28, Sweden;* ⓞ orcid.org/0000-0002-0168-2942

Complete contact information is available at:
https://pubs.acs.org/10.1021/acsaem.3c02242

Author Contributions

A.S., L.K., and P.H.S. contributed to the idea and experimental design. A.S. performed the major part of the experimental work. L.K. performed the theoretical calculations. P.H.S. performed the SXRD crystal structure analysis. L.K and P.H.S. supervised the project. A.S. wrote the initial manuscript draft. All authors contributed to the discussion of content and assisted in editing the manuscript before submission.

Notes

The authors declare no competing financial interest.

■ ACKNOWLEDGMENTS

■ REFERENCES

(1) National Renewable Energy Laboratory *Best Research-Cell Efficiencies*; https://www.nrel.gov/pv/assets/pdfs/best-research-cell-efficiencies.20200104.pdf (accessed: **2021-01−09**).

(2) Akkerman, Q. A.; Manna, L. What Defines a Halide Perovskite? *ACS Energy Lett.* **2020**, *5*, 604−610.

(3) Correa-Baena, J.-P.; Saliba, M.; Buonassisi, T.; Grätzel, M.; Abate, A.; Tress, W.; Hagfeldt, A. Promises and challenges of perovskite solar cells. *Science* **2017**, *358*, 739−744.

(4) Kojima, A.; Teshima, K.; Shirai, Y.; Miyasaka, T. Organ metal Halide Perovskites as Visible-Light Sensitizers for Photovoltaic Cells. *J. Am. Chem. Soc.* **2009**, *131*, 6050−6051.

(5) Espinosa, N.; Serrano-Luján, L.; Urbina, A.; Krebs, F. C. Solution and vapour deposited lead perovskite solar cells: Ecotoxicity from a life cycle assessment perspective. *Sol. Energy Mater. Sol. Cells* **2015**, *137*, 303−310.

(6) Bae, S.-Y.; Lee, S. Y.; Kim, J.-W.; Umh, H. N.; Jeong, J.; Bae, S.; Yi, J.; Kim, Y.; Choi, J. Hazard potential of perovskite solar cell technology for potential implementation of "safe-by-design" approach. *Sci. Rep.* **2019**, *9*, 4242.

(7) Mitchell, S. C.; Zhang, A. Q. Methylamine in Human Urine. *Clin. Chem. Acta.* **2001**, *312*, 107−114.

(8) Guest, I.; Varma, D. R. Developmental toxicity of methylamines in mice. *J. Toxicol. Environ. Health.* **1991**, *32*, 319−330.

(9) Hailegnaw, B.; Kirmayer, S.; Edri, E.; Hodes, G.; Cahen, D. Rain on Methylammonium Lead Iodide Based Perovskites: Possible Environmental Effects of Perovskite Solar Cells. *J. Phys. Chem. Lett.* **2015**, *6*, 1543−1547.

(10) Li, X.; Zhang, F.; He, H.; Berry, J. J.; Zhu, K.; Xu, T. On-device lead sequestration for perovskite solar cells. *Nature.* **2020**, *578*, 555−558.

(11) Berry, J.; Buonassisi, T.; Egger, D. A.; Hodes, G.; Kronik, L.; Loo, Y. L.; Lubomirsky, I.; Marder, S. R.; Mastai, Y.; Miller, J. S.; Mitzi, D. B.; Paz, Y.; Rappe, A. M.; Riess, I.; Rybtchinski, B.; Stafsudd, O.; Stevanovic, V.; Toney, M. F.; Zitoun, D.; Kahn, A.; Ginley, D.; Cahen, D. Hybrid Organic−Inorganic Perovskites (HOIPs): Opportunities and Challenges. *Adv. Mater.* **2015**, *27*, 5102−5112.

(12) Zhang, X.; Chen, X.; Chen, Y.; Aida, N.; Ouedraogo, N.; Li, J.; Bao, X.; Han, C. B.; Shirai, Y.; Zhang, Y.; Yan, H. Rapid degradation behavior of encapsulated perovskite solar cells under light, bias voltage or heat fields. *Nanoscale Adv.* **2021**, *3*, 6128−6137.

(13) Han, Y.; Meyer, S.; Dkhissi, Y.; Weber, K.; Pringle, J. M.; Bach, U.; Spiccia, L.; Cheng, Y.-B. Degradation observations of encapsulated planar CH$_3$NH$_3$PbI$_3$ perovskite solar cells at high temperatures and humidity. *J. Mater. Chem. A* **2015**, *3*, 8139−8147.

(14) Philippe, B.; Park, B.-W.; Lindblad, R.; Oscarsson, J.; Ahmadi, S.; Johansson, E. M.; Rensmo, H. K. Chemical and Electronic Structure Characterization of Lead Halide Perovskites and Stability Behavior under Different Exposures—A Photoelectron Spectroscopy Investigation. *Chem. Mater.* **2015**, *27*, 1720−1731.

(15) Juarez-Perez, E. J.; Ono, L. K.; Maeda, M.; Jiang, Y.; Hawash, Z.; Qi, Y. Photodecomposition and thermal decomposition in methylammonium halide lead perovskites and inferred design principles to increase photovoltaic device stability. *J. Mater. Chem. A* **2018**, *6*, 9604−9612.

(16) Davies, M. L. Addressing the Stability of Lead Halide Perovskites. *Joule* **2020**, *4*, 1626−1636.

(17) Ke, W.; Kanatzidis, M. G. Prospects for low-toxicity lead-free perovskite solar cells. *Nat. Commun.* **2019**, *10*, 965.

(18) Cao, J.; Yan, F. Recent progress in tin-based perovskite solar cells. *Energy Environ. Sci.* **2021**, *14*, 1286−1325.

(19) Ganose, A. M.; Savory, C. N.; Scanlon, D. O. Beyond methylammonium lead iodide: prospects for the emergent field of ns² containing solar absorbers. *Chem. Commun.* **2017**, *53*, 20−44.

(20) Jiang, Y.; Qiu, L.; Juarez-Perez, E. J.; Ono, L. K.; Hu, Z.; Liu, Z.; Wu, Z.; Meng, L.; Wang, Q.; Qi, Y. Reduction of lead leakage from damaged lead halide perovskite solar modules using self-healing polymer-based encapsulation. *Nat. Energy* **2019**, *4*, 585−593.

(21) Jiang, Q.; Zhao, Y.; Zhang, X.; Yang, X.; Chen, Y.; Chu, Z.; Ye, Q.; Li, X.; Yin, Z.; You, J. Surface passivation of perovskite film for efficient solar cells. *Nat. Photonics* **2019**, *13*, 460−466.

(22) Min, X.; Pengchen, Z.; Gu, S.; Jia, Z. Research progress of low-dimensional perovskites: synthesis, properties and optoelectronic applications. *J. Semicond.* **2017**, *38*, No. 011004.

(23) Zhu, P.; Zhu, J. Low-dimensional metal halide perovskites and related optoelectronic applications. *InfoMater.* **2020**, *2*, 341−378.

(24) Chen, P.; Bai, Y.; Lyu, M.; Yun, J.-H.; Hao, M.; Wang, L. Progress and Perspective in Low-Dimensional Metal Halide Perovskites for Optoelectronic Applications. *Sol. RRL* **2018**, *2*, No. 1700186.

(25) Wolf, N. R.; Connor, B. A.; Slavney, A. H.; Karunadasa, H. I. Doubling the Stakes: The Promise of Halide Double Perovskites. *Angew. Chem., Int. Ed.* **2021**, *60*, 16264−16278.

(26) Goldschmidt, V. M. Die Gesetze der Krystallochemie. *Naturwissenschaften* **1926**, *14*, 477−485.

(27) Mao, L.; Stoumpos, C. C.; Kanatzidis, M. G. Two-Dimensional Hybrid Halide Perovskites: Principles and Promises. *J. Am. Chem. Soc.* **2019**, *141*, 1171−1190.

(28) Koutselas, I. B.; Ducasse, L.; Papavassiliou, G. C. Electronic properties of three- and low-dimensional semiconducting materials with Pb halide and Sn halide units. *J. Phys.: Condens. Matter* **1996**, *8*, 1217.

(29) Kamminga, M. E.; Fang, H.-H.; Filip, M. R.; Giustino, F.; Baas, J.; Blake, G. R.; Loi, M. A.; Palstra, T. T. M. Confinement Effects in Low-Dimensional Lead Iodide Perovskite Hybrids. *Chem. Mater.* **2016**, *28*, 4554−4562.

(30) Tabor, D. P.; Roch, L. M.; Saikin, S. K.; Kreisbeck, C.; Sheberla, D.; Montoya, J. H.; Dwaraknath, S.; Aykol, M.; Ortiz, C.; Tribukait, H.; Amador-Bedolla, C.; Brabec, C. J.; Maruyama, B.; Persson, K. A.; Aspuru-Guzik, A. Accelerating the discovery of materials for clean energy in the era of smart automation. *Nat. Rev. Mater.* **2018**, *3*, 5−20.

(31) Wagner, J.; Berger, C. G.; Du, X.; Stubhan, T.; Hauch, J. A.; Brabec, C. J. The evolution of Materials Acceleration Platforms: toward the laboratory of the future with AMANDA. *J. Mater. Sci.* **2021**, *56*, 16422−16446.

(32) Gross, R.; Hanna, R.; Gambhir, A.; Heptonstall, P.; Speirs, J. How long does innovation and commercialisation in the energy sectors take? Historical case studies of the timescale from invention to widespread commercialisation in energy supply and end use technology. *Energy Policy* **2018**, *123*, 682−699.

(33) Gu, E.; Tang, X.; Langner, S.; Duchstein, P.; Zhao, Y.; Levchuk, I.; Kalancha, V.; Stubhan, T.; Hauch, J.; Egelhaaf, H. J.; Zahn, D.; Osvet, A.; Brabec, C. J. Robot-Based High-Throughput Screening of Antisolvents for Lead Halide Perovskites. *Joule* **2020**, *4*, 1806−1822.

(34) Sun, S.; Hartono, N. T. P.; Ren, Z. D.; Oviedo, F.; Buscemi, A. M.; Layurova, M.; Chen, D. X.; Ogunfunmi, T.; Thapa, J.; Ramasamy, S.; Settens, C.; DeCost, B. L.; Kusne, A. G.; Liu, Z.; Tian, S. I. P.; Peters, I. M.; Correa-Baena, J.-P.; Buonassisi, T. Accelerated Development of Perovskite-Inspired Materials via High-Throughput Synthesis and Machine-Learning Diagnosis. *Joule* **2019**, *3*, 1437−1451.

(35) Li, Z.; Najeeb, M. A.; Alves, L.; Sherman, A. Z.; Shekar, V.; Cruz Parrilla, P.; Pendleton, I. M.; Wang, W.; Nega, P. W.; Zeller, M.; Schrier, J.; Norquist, A. J.; Chan, E. M. Robot-Accelerated Perovskite Investigation and Discovery. *Chem. Mater.* **2020**, *32*, 5650−5663.

(36) Kirman, J.; Johnston, A.; Kuntz, D. A.; Askerka, M.; Gao, Y.; Todorovic, P.; Ma, D.; Prive, G. G.; Sargent, E. H. Machine-Learning-Accelerated Perovskite Crystallization. *Matter* **2020**, *2*, 938−947.

(37) Starkholm, A.; Kloo, L.; Svensson, P. H. Implicit Tandem Organic−Inorganic Hybrid Perovskite Solar Cells Based on Internal Dye Sensitization: Robotized Screening, Synthesis, Device Implementation, and Theoretical Insights. *J. Am. Chem. Soc.* **2020**, *142*, 18437−18448.

(38) Mishra, A.; Ahmad, Z. Potential challenges and approaches to develop the large area efficient monolithic perovskite solar cells (mPSCs). *J. Mater. Sci. Mater. Electron* **2019**, *30*, 20320−20329.

(39) Meroni, S. M. P.; Worsley, C.; Raptis, D.; Watson, T. M. Triple-Mesoscopic Carbon Perovskite Solar Cells: Materials, Processing and Applications. *Energies* **2021**, *14*, 386.

(40) Per, S. Solar Cell Screening 2. YouTube https://www.youtube.com/watch?v=GjVb_QXw7_k (Accessed **2022-12−15**).

(41) Starkholm, A.; Kloo, L.; Svensson, P. H. Gold Polyiodide Hybrid Perovskite Solar Cells. *ACS Materials Lett.* **2023**, *5*, 406−412.

(42) Starkholm, A. Synthesis and Robotized Screening of Novel Perovskite Materials for Solar Cell Application. PhD Thesis; KTH Royal Institute of Technology: Stockholm, Sweden, 2021.

(43) *Bruker Apex II*, 2013.2−0; Bruker AXS: Madison, WI, 2013.

(44) Sheldrick, G. A short history of SHELX. *Acta Crystallogr. A* **2008**, *64*, 112−122.

(45) Dovesi, R.; Erba, A.; Orlando, R.; Zicovich-Wilson, C. M.; Civalleri, B.; Maschio, L.; Rerat, M.; Casassa, S.; Baima, J.; Salustro, S.; Kirtman, B. Quantum-mechanical condensed matter simulations with CRYSTAL. *WIREs Comp. Mol. Sci.* **2018**, *8*, No. e1360.

(46) Stoll, H.; Metz, B.; Dolg, M. Relativistic energy-consistent pseudopotentials—Recent developments. *J. Comput. Chem.* **2002**, *23*, 767−778.

(47) Metz, B.; Stoll, H.; Dolg, M. Small-core multiconfiguration-Dirac−Hartree−Fock-adjusted pseudopotentials for post-d main group elements: Application to PbH and PbO. *J. Chem. Phys.* **2000**, *113*, 2563−2569.

(48) Peterson, K. A.; Shepler, B. C.; Figgen, D.; Stoll, H. On the Spectroscopic and Thermochemical Properties of ClO, BrO, IO, and Their Anions. *J. Phys. Chem. A* **2006**, *110*, 13877−13883.

(49) Peterson, K. A. Systematically convergent basis sets with relativistic pseudopotentials. I. Correlation consistent basis sets for the post-d group 13−15 elements. *J. Chem. Phys.* **2003**, *119*, 11099−11112.

(50) Bergner, A.; Dolg, M.; Küchle, W.; Stoll, H.; Preuss, H. Ab initio energy-adjusted pseudopotentials for elements of groups 13−17. *Mol. Phys.* **1993**, *80*, 1431−1441.

(51) CRYSPLOT online visualization tool; Available via the internet at: http://crysplot.crystalsolutions.eu/. Accessed **2021-10−15**.

(52) Frisch, M. J.; Trucks, G. W.; Schlegel, H. B.; Scuseria, G. E.; Robb, M. A.; Cheeseman, J. R.; Scalmani, G.; Barone, V.; Mennucci, B.; Petersson, G. A.; Nakatsuji, H.; Caricato, M.; Li, X.; Hratchian, H. P.; Izmaylov, A. F.; Bloino, J.; Zheng, G.; Sonnenberg, J. L.; Hada, M.; Ehara, M.; Toyota, K.; Fukuda, R.; Hasegawa, J.; Ishida, M.; Nakajima, T.; Honda, Y.; Kitao, O.; Nakai, H.; Vreven, T.; Montgomery, J. A., Jr.; Peralta, J. E.; Ogliaro, F.; Bearpark, M.; Heyd, J. J.; Brothers, E.; Kudin, K. N.; Staroverov, V. N.; Kobayashi, R.; Normand, J.; Raghavachari, K.; Rendell, A.; Burant, J. C.; Iyengar, S. S.; Tomasi, J.; Cossi, M.; Rega, N.; Millam, J. M.; Klene, M.; Knox, J. E.; Cross, J. B.; Bakken, V.; Adamo, C.; Jaramillo, J.; Gomperts, R.; Stratmann, R. E.; Yazyev, O.; Austin, A. J.; Cammi, R.; Pomelli, C.; Ochterski, J. W.; Martin, R. L.; Morokuma, K.; Zakrzewski, V. G.; Voth, G. A.; Salvador, P.; Dannenberg, J. J.; Dapprich, S.; Daniels, A. D.; Farkas, O.; Foresman, J. B.; Ortiz, J. V.; Cioslowski, J.; Fox, D. J. *Gaussian 16, Rev. B.01*; Gaussian, Inc.: Wallingford, CT, 2016.